

Near-field aeroacoustic characteristics of a stalled NACA 0012 airfoil

Yannick D. Mayer*, B. Zang†, Mahdi Azarpeyvand‡

Faculty of Engineering, University of Bristol, United Kingdom

ABSTRACT

Stall and separation noise can be major contributors to the noise emission of rotating blades, such as wind turbines, propellers and fans among others. Hence, this paper experimentally investigates the effects a separated boundary layer has on near-field flow structures, on turbulent surface pressure fluctuation statistics, and therefore on noise radiation. Static pressure distributions and boundary layer profiles are presented to characterize the present flow fields pre- and post-stall. Large surface pressure fluctuation spectra increases have been measured, and surface pressure fluctuation autocorrelation width increases by one order of magnitude during stall have been established. Additionally, highly coherent spanwise structures have been shown to influence the hydrodynamic field and changes in the convection velocity have been assessed for separated boundary layers.

Keywords: Aeroacoustics, Separation and Stall Noise, Surface Pressure Fluctuations, Convection Velocity, Flow Separation.

1 INTRODUCTION

Brooks *et al.* reported five different airfoil self-noise mechanisms (1). For the majority of today's industrial applications, the most relevant self-noise mechanisms are turbulent boundary layer trailing edge noise, laminar boundary layer vortex shedding noise and separation/stall noise. Trailing-edge noise and laminar vortex shedding noise have been the subject of many studies over the years (1–7), but stall/separation noise investigations are comparably limited. This is despite stall noise being assumed to be a significant contributor to wind turbine noise emissions due to sudden changes in environmental conditions, such as gust or topographical effects for instance (8, 9). Since computational stall noise investigations require a substantial spanwise domain to achieve sufficient de-correlation of the present flow structures (10), the majority of stall noise studies have been of experimental nature, for instance by Moreau *et al.* (11), Mayer *et al.* (12), Bertagnolio *et al.* (13) and Laratro *et al.* (14) among others. The experimental results clearly point toward a shift to low frequency noise emissions and considerable low frequency surface pressure spectra increases.

This paper aims to further experimentally examine and characterize the hydrodynamic near-field during stall. Section 2 will introduce the experimental setup as well as the utilized symmetric airfoil, before unsteady surface pressure fluctuation and hot wire results are presented in Section 3. Lastly, Section 4 will provide conclusions and an outlook on future work.

*Ph.D. Researcher Aerospace Engineering, yannick.mayer@bristol.ac.uk.

†Research Associate Aerospace Engineering, nick.zang@bristol.ac.uk.

‡Corresponding Author, Reader in Aeroacoustics, m.azarpeyvand@bristol.ac.uk.

2 EXPERIMENTAL SETUP

2.1 Overview

Experiments were conducted in the aeroacoustic wind tunnel facility of the University of Bristol (15). An overview of the experimental setup and a rendering of the anechoic chamber are shown in Fig. 1. This study used a nozzle with the exit dimensions of 500 mm width and 775 mm height at a free stream velocity of $U_\infty = 20 \text{ m s}^{-1}$, corresponding to a chord-based Reynolds number of $Re_c = 4.0 \cdot 10^5$ for the utilized NACA 0012 airfoil. A 1500 mm long test section with tensioned Kevlar cloth at the top and bottom is employed in order to limit excessive flow deflection, while permitting acoustic sound waves to pass through with little attenuation. Mayer *et al.* characterized this Kevlar-walled test section acoustically as well as aerodynamically and showed that geometric angles of attack can be corrected to the equivalent free-stream angle of attack (16). Each of the two vertical sides has three perspex windows allowing test objects and measurement equipment to be installed or inserted. Neoprene strips and insulation tape have been used throughout to avoid any extraneous noise sources such as air leaks, gaps or cavities. The angle of attack of the NACA 0012 airfoil with a chord length of 300 mm is controlled by a high torque servo motor.

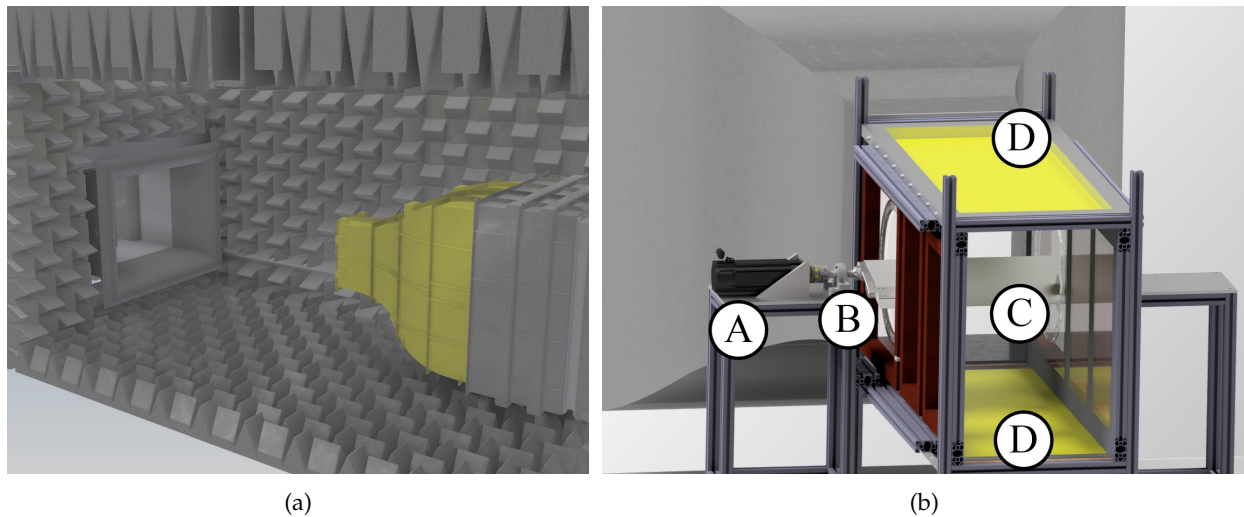


Figure 1. (a) Anechoic chamber and (b) Isometric rendering of the experimental setup: (A) servo motor, (B) coupling and bearing, (C) NACA 0012 airfoil and (D) tensioned Kevlar cloth.

2.2 NACA 0012 airfoil

The NACA 0012 airfoil has a chord length of $c = 300 \text{ mm}$ and it is tripped by a 6 mm wide and 0.5 mm thick zig-zag turbulator trip tape from Glasfaser-Flugzeug-Service GmbH (17), located at approximately 13% of the chord on both airfoil sides. The airfoil is equipped with 87 static pressure taps together with 91 embedded microphones placed under 0.4 mm diameter pinholes, of which 21 are operated in a remote sensing configuration. Both the static pressure taps and unsteady pressure transducers are aligned along the chord as well as along the span at several chordwise locations. Knowles FG-23629-P16 microphones are used as the in-situ direct sensing microphone and Panasonic WM-61A microphones are used for the remote sensing configurations. All microphones were calibrated in magnitude and phase referenced to a G.R.A.S. 40PL microphone.

2.3 Data acquisition and postprocessing

All microphone and hot wire measurements were sampled simultaneously at a frequency of 2^{15} Hz for 32 s using five 16-channel NI PXIe-4499 modules mounted in a NI PXIe-1062Q chassis. All microphone signals are zero-phase high-pass filtered at 20 Hz, to account for the low-frequency limit of both microphones. A Dantec 55P15 boundary layer hot wire probe was traversed using two Thorlabs LTS300 stages and operated via a CTA91C10 module. The probe was calibrated daily using a Dantec 54H10 calibrator. The power spectral density of the surface pressure fluctuations, ϕ_{pp} , is estimated via Welch's method using a window size of 2^{11} samples and a Hamming window with 50% overlap, resulting in a frequency bin size of 16 Hz. All surface pressure spectra are normalized with a reference pressure of $p_0 = 20 \mu\text{Pa}$. Lastly, 64 static pressure taps were simultaneously connected to two MicroDaq-32 pressure acquisition systems, manufactured by Chell, and data are recorded at 1000 Hz for a duration of 32 s.

3 RESULTS AND DISCUSSION

This section will present test results including static surface pressure results, unsteady surface pressure results and hot wire anemometry results. The geometric angle of attack, α , was altered from -5° to 23° in increments of $\alpha = 0.5^\circ$. However, this conference paper will mainly focus on one pre-stall angle of attack, $\alpha = 12^\circ$, and one post-stall angle of attack, $\alpha = 15^\circ$.

3.1 Pressure distribution

Figure 2 displays the mean static pressure coefficient for five angles of attack up to $\alpha = 15^\circ$. As the angle of attack is increased, the suction side pressure peak increases and shifts toward the leading edge, as expected, and for $\alpha = 10^\circ$ and $\alpha = 12^\circ$ a laminar separation bubble is evidently present near the leading edge due to a strong adverse pressure gradient. At $\alpha = 15^\circ$, the boundary layer has separated near the leading edge and the pressure distribution is effectively constant for the suction side, confirming a sudden leading-edge type stall behavior. Additionally, the effect of the trip strip is clearly visible except for $\alpha = 15^\circ$.

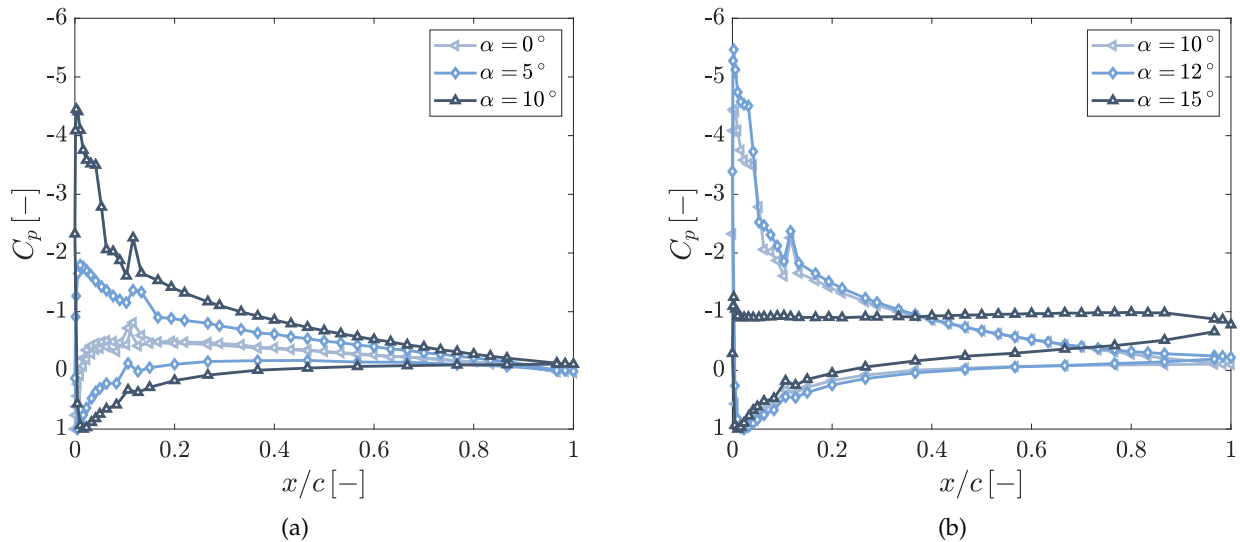


Figure 2. Static pressure coefficient, C_p , distribution at $Re_c = 4.0 \cdot 10^5$: (a) 0° to 10° and (b) 10° to 15° .

3.2 Boundary layer measurements

This section presents single-wire hot wire measurements for varying airfoil wall normal distances (z_w), namely mean velocity and velocity fluctuation profiles normalized with the boundary layer edge velocity, U_e , in Fig. 3 up to $\alpha = 15^\circ$. It is illustrated that the boundary layer thickness increases for increasing angle of attack. Once, the boundary layer has separated at $\alpha = 15^\circ$, the velocity profile suggests that up to $z_w/c = 0.22$, a reverse flow is present, because of the plateau in the velocity distribution up to $z_w/c = 0.22$ (18). Additionally, the peak of the surface pressure fluctuations has moved away from the airfoil surface, increased in magnitude and now occurs at $z_w/c = 0.32$, while the extent of the separated boundary layer approaches half the airfoil chord length.

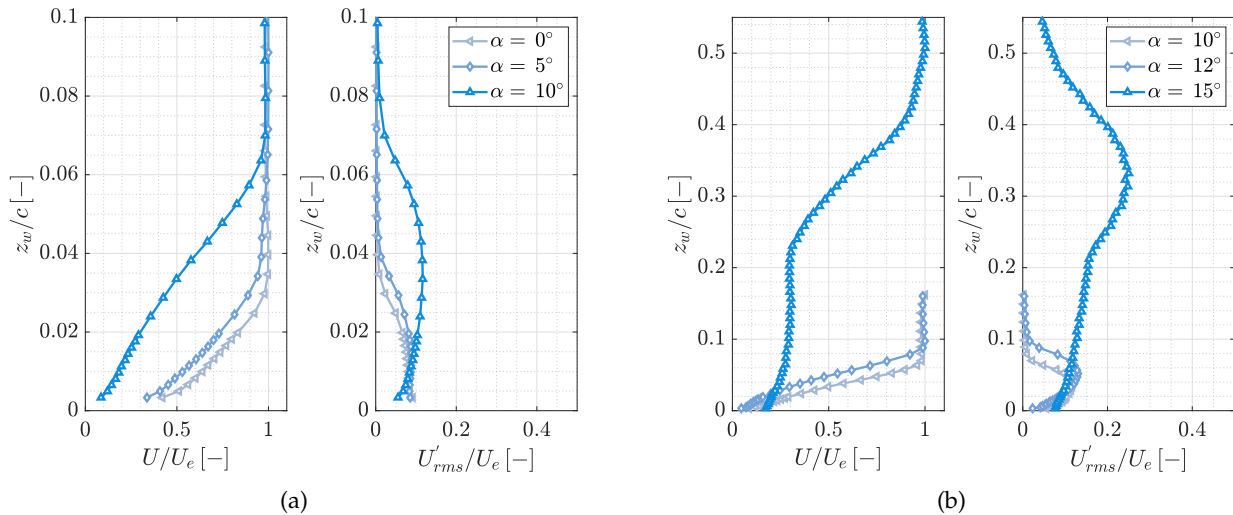


Figure 3. Boundary layer measurement at $x/c = 0.98$: (a) $\alpha = 0^\circ$ to 10° and (b) $\alpha = 10^\circ$ to 15° .

3.3 Surface pressure fluctuation PSD

The remaining sections examine the unsteady surface pressure fluctuations as measured by the embedded microphones. This particular section focuses on power spectral density (PSD) of the unsteady surface pressure fluctuations to examine the energy distribution in the frequency domain.

Figure 4 presents the surface pressure spectra near the leading edge at $x/c = 0.3$ and near the trailing edge at $x/c = 0.99$. For both pressure transducer locations the peak frequency shift to lower frequencies for increasing angles of attack is clear, as the peak spectrum value also increases from 65 dB to 95 dB and from 70 dB to 101 dB for $x/c = 0.3$ and $x/c = 0.99$, respectively. The frequency shifts and spectra increases occur as a result of a growing boundary layer and subsequent flow separation due to the adverse pressure gradient on the suction side of the airfoil. A thicker boundary layer results in larger length scales in the flow, which in turn leads to lower peak frequencies. It is noticeable that the most significant change occurs between $\alpha = 12^\circ$ and $\alpha = 15^\circ$, highlighting the profound effect stall has on the surface pressure spectra. This rapid and abrupt change can also be observed in Fig. 5, showing contour plots of the surface pressure fluctuation spectra up to $\alpha = 15^\circ$ for transducers covering the space between $x/c = 0.3$ and $x/c = 0.99$.

3.4 Surface pressure autocorrelation

The autocorrelation coefficient width, $R_{pp}(\tau)$ (where τ is the time delay), is indicative of the size of the dominant flow structures causing the surface pressure fluctuations. Figure 6 displays a contour map of the variation of the autocorrelation coefficient along the suction side of the airfoil for $\alpha = 12^\circ$ and $\alpha = 15^\circ$, with the

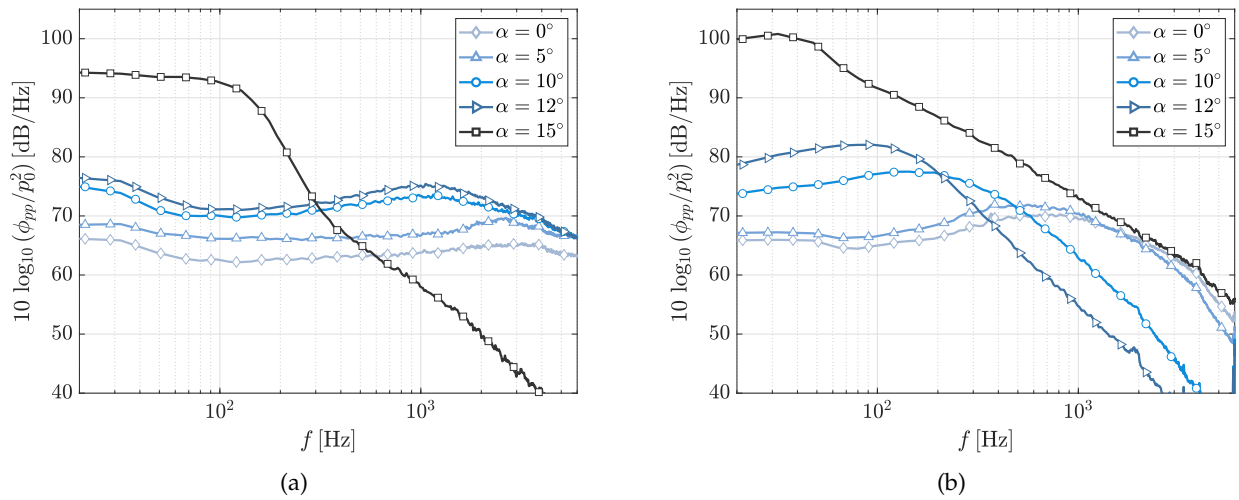


Figure 4. Wall pressure fluctuation PSD for various angles of attack: (a) $x/c = 0.3$ and (b) $x/c = 0.99$.

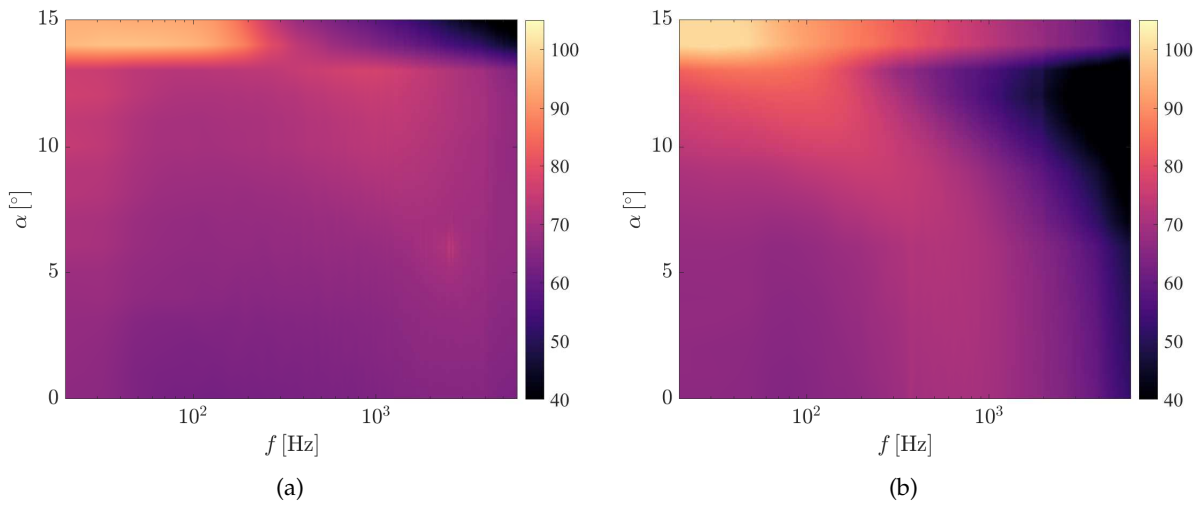


Figure 5. Wall pressure fluctuation PSD contour plot: (a) $x/c = 0.3$ and (b) $x/c = 0.99$.

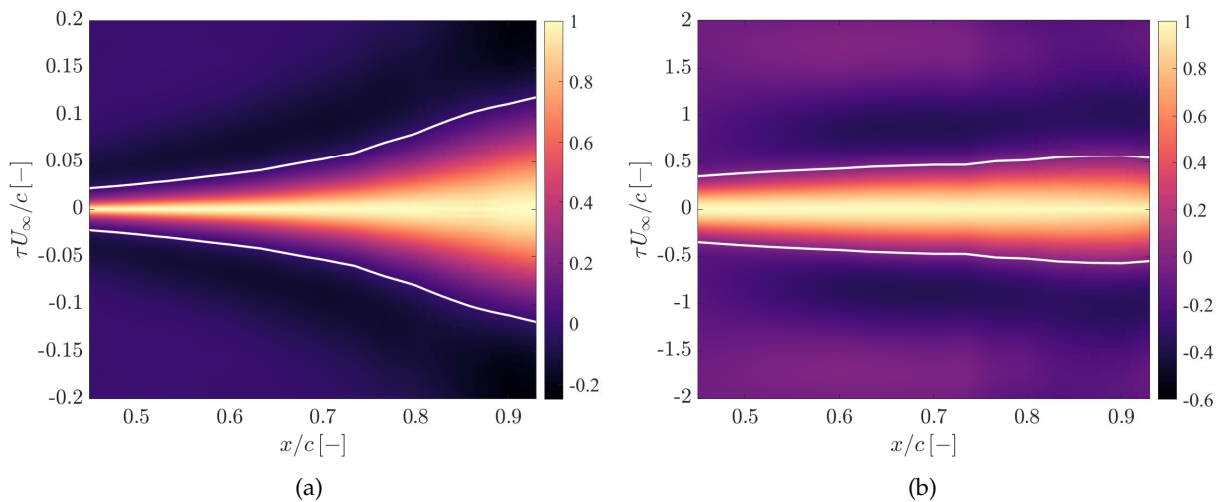


Figure 6. Wall pressure fluctuation autocorrelation, R_{pp} , contour maps: (a) $\alpha = 12^\circ$ and (b) $\alpha = 15^\circ$. First zero crossing is displayed as a white line.

white line displaying the first zero-crossing of the autocorrelation coefficient. At $\alpha = 12^\circ$, the autocorrelation width increases strongly toward the trailing edge due to the strong adverse pressure gradient resulting in a thicker boundary layer, see Figs. 2 and 3. This trend is in stark contrast to the contour map at $\alpha = 15^\circ$, because the autocorrelation width is approximately one order of magnitude larger in comparison, but shows less variation along the chord. This therefore suggests that the dominant flow structures have undoubtedly increased in size, and occur over a large extent of the airfoil without significantly evolving or changing in size.

3.5 Surface pressure spanwise coherence

Figure 7 displays the spanwise coherence spectra, γ^2 , for seven pressure transducers located at $x/c = 0.70$. On the one hand, it can be observed that at $\alpha = 12^\circ$ the coherence spectra reach considerable values for the sensor separation distances of up to $\xi_2/c = 0.047$ and the spectra reach local maxima at approximately 200 Hz. On the other hand, at $\alpha = 15^\circ$, substantial coherence values are observed even for the largest sensor separation distance of $\xi_2/c = 0.243$, and for separation distances of up to $\xi_2/c = 0.047$, the coherence for frequencies below 100 Hz almost reaches unity. This coherence increase can be interpreted as the occurrence of spanwise highly coherent flow structures which are supported by the large vertical extent of the separation region.

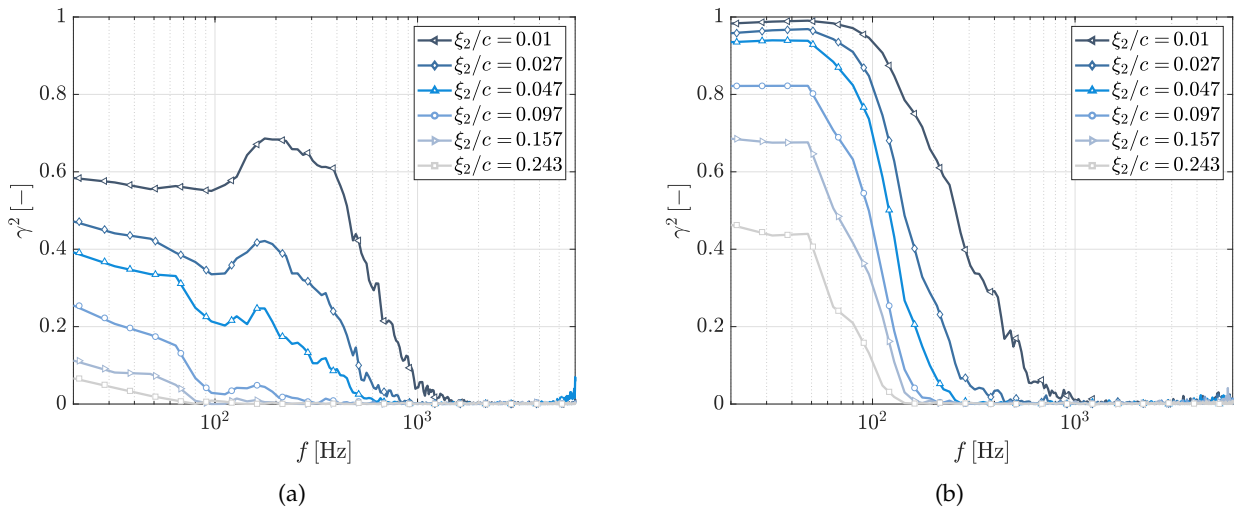


Figure 7. Wall pressure fluctuation coherence, γ^2 , for multiple spanwise distances, ξ_2 , at $x/c = 0.70$: (a) $\alpha = 12^\circ$ and (b) $\alpha = 15^\circ$.

3.6 Surface pressure cross-correlation

This section concerns the cross-correlation coefficient between the surface pressure fluctuations at varying chordwise distances, ξ_1 , allowing the determination of the convection velocity, U_c , of the most prominent flow structures, as

$$\frac{U_c}{U_\infty} = \frac{\xi_1/c}{\tau_{max} U_\infty/c}, \quad (1)$$

where τ_{max} is the time delay with the maximum cross-correlation coefficient. Figure 8 displays the chordwise cross-correlation coefficient referenced to the pressure transducer located at $x/c = 0.93$, while Table 1 lists the corresponding convection velocities, calculated via Eq. 1. It is apparent that for $\alpha = 0^\circ$ and 10° , the convection velocity increases for greater sensor separation distances, because the larger flow structures which travel further away from the airfoil surface have longer live spans and are convected at larger surface normal

Table 1. Serration parameters.

Sensor separation distance, ξ_1/c [-]	U_c/U_∞ for $\alpha = 0^\circ$ [-]	U_c/U_∞ for $\alpha = 12^\circ$ [-]	U_c/U_∞ for $\alpha = 15^\circ$ [-]
0.033	0.63	0.53	-0.78
0.050	0.64	0.56	2.73
0.067	0.70	0.56	0.94
0.083	0.72	0.59	0.72
0.100	0.72	0.60	0.62

distances. The highest convection velocity at $\alpha = 0^\circ$ is $U_c/U_\infty = 0.72$ and $U_c/U_\infty = 0.60$ for $\alpha = 12^\circ$, suggesting a decrease with increasing angles of attack as long as the boundary layer stays attached. However, in stalled conditions, *i.e.* $\alpha = 15^\circ$, the convection velocity is calculated to be negative for the smallest sensor spacing of $\xi_1/c = 0.033$ and finally reaches $U_c/U_\infty = 0.62$ for the greatest separation distance investigated here.

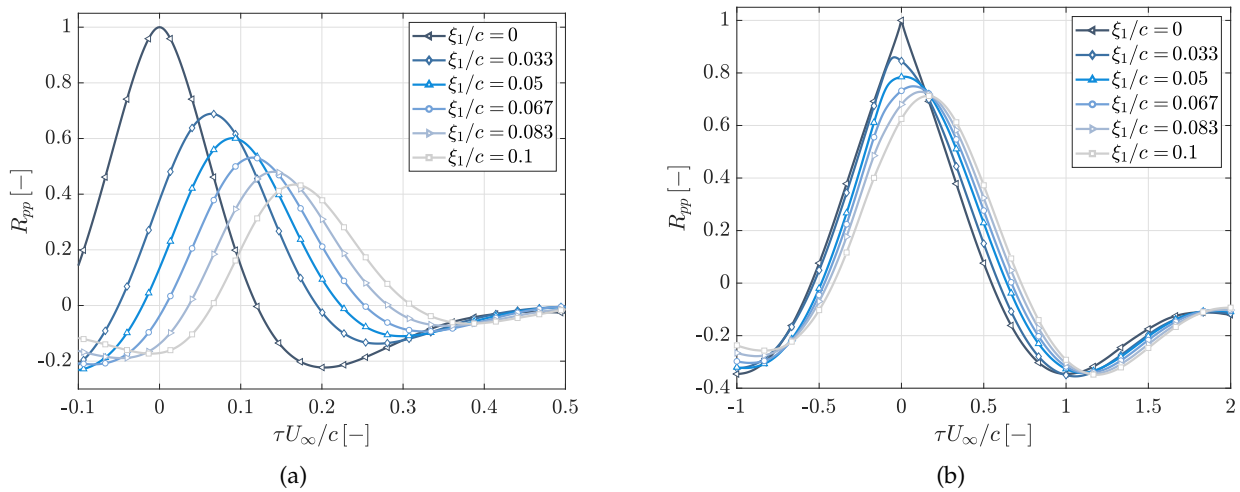


Figure 8. Wall pressure fluctuation cross-correlation, R_{pp} , for various sensor separation distances, with the reference sensor located at $x/c = 0.93$: (a) $\alpha = 12^\circ$ and (b) $\alpha = 15^\circ$.

4 FINAL REMARKS

This paper investigated the effect of flow separation on near-field aeroacoustic properties, such as surface pressure spectra and convection velocity. Substantial and sudden increases were found in both surface pressure spectra and autocorrelation widths once the boundary layer had separated. Additionally, locally negative convection velocities and a decrease in the convection velocity were established in the presence of flow separation. The results provided in this paper are a small snapshot of the total data set available from the highly instrumented airfoil.

Future investigations will include further flow field characterizations using dual sensor hot wire probes, higher order analysis of the surface pressure fluctuations, as well as far-field noise studies. In addition, dynamic stall noise and stall noise mitigation approaches will be examined.

ACKNOWLEDGEMENTS

The first author gratefully acknowledges the financial support of the ICA-ASA-DEGA Young Scientists Conference Grant and all authors acknowledge the support of the Engineering and Physical Sciences Research Council (EPSRC Grant No. EP/R010846/1).

REFERENCES

- [1] Thomas F. Brooks, D. Stuart Pope, and Michael A. Marcolini. Airfoil Self-Noise and Prediction. Technical report, NASA Langley Research Center, Hampton, Virginia, United States, 1989.
- [2] Christopher K. W. Tam. Discrete tones of isolated airfoils. *The Journal of the Acoustical Society of America*, 55(6): 1173–1177, 1974. doi: 10.1121/1.1914682.
- [3] Bin Zang, Yannick D. Mayer, and Mahdi Azarpeyvand. An Experimental Investigation on the Mechanism of Tollmien-Schlichting Waves for a NACA 0012 Aerofoil. In *25th AIAA/CEAS Aeroacoustics Conference*, AIAA 2019-2609, Delft, The Netherlands, 2019. doi: 10.2514/6.2019-2609.
- [4] S Pröbsting, F Scarano, and S C Morris. Regimes of tonal noise on an airfoil at moderate Reynolds number. *Journal of Fluid Mechanics*, 780:407–438, 2015. doi: 10.1017/jfm.2015.475.
- [5] M. S. Howe. A Review of the Theory of Trailing Edge Noise. *Journal of Sound and Vibration*, 61(3):437–465, 1978.
- [6] Tze Pei Chong and Alexandros Vathylakis. On the aeroacoustic and flow structures developed on a flat plate with a serrated sawtooth trailing edge. *Journal of Sound and Vibration*, 354:65–90, 2015. doi: 10.1016/j.jsv.2015.05.019.
- [7] Yannick D. Mayer, Benshuai Lyu, Hasan Kamliya Jawahar, and Mahdi Azarpeyvand. A semi-analytical noise prediction model for airfoils with serrated trailing edges. *Renewable Energy*, 143:679–691, 2019. doi: 10.1016/j.renene.2019.04.132.
- [8] Alex Laratro, Maziar Arjomandi, Richard Kelso, and Benjamin Cazzolato. A discussion of wind turbine interaction and stall contributions to wind farm noise. *Journal of Wind Engineering and Industrial Aerodynamics*, 127:1–10, 2014. doi: 10.1016/j.jweia.2014.01.007.
- [9] S Oerlemans. An explanation for enhanced amplitude modulation of wind turbine noise. Technical Report NLR-CR-2011-071, National Aerospace Laboratory, Amsterdam, Netherlands, 2011.
- [10] Joseph G. Kocheemoolayil and Sanjiva K. Lele. Large Eddy Simulation of Airfoil Self-Noise at High Reynolds Number. In *22nd AIAA/CEAS Aeroacoustics Conference*, AIAA2016-2919, AIAA 2016-2919, Lyon, France, 2016. doi: 10.2514/6.2016-2919.
- [11] Stéphane Moreau, Michel Roger, and Julien Christophe. Flow Features and Self-Noise of Airfoils Near Stall or in Stall. In *15th AIAA/CEAS Aeroacoustics Conference (30th AIAA Aeroacoustics Conference)*, AIAA 2009-3198, Miami, Florida, United States, 2009.
- [12] Yannick D. Mayer, B Zang, and Mahdi Azarpeyvand. Aeroacoustic Characteristics of a NACA 0012 Airfoil for Attached and Stalled Flow Conditions. In *25th AIAA/CEAS Aeroacoustics Conference*, AIAA 2019-2530, Delft, The Netherlands, 2019. doi: 10.2514/6.2019-2530.
- [13] Franck Bertagnolio, Helge Aagaard Madsen, Andreas Fischer, and Christian Bak. Experimental Characterization of Stall Noise Toward its Modelling. *Proceedings of the 6th International Conference on Wind Turbine Noise*, 2015.
- [14] Alex Laratro, Maziar Arjomandi, Benjamin Cazzolato, and Richard Kelso. Self-noise of NACA 0012 and NACA 0021 aerofoils at the onset of stall. *International Journal of Aeroacoustics*, 16(3):181–195, 2017. doi: 10.1177/1475472X17709929.
- [15] Yannick D. Mayer, Hasan Kamliya Jawahar, Mate Szöke, and Mahdi Azarpeyvand. Design of an Aeroacoustic Wind Tunnel Facility at the University of Bristol. In *2018 AIAA/CEAS Aeroacoustics Conference*, AIAA 2018-3138, Atlanta, Georgia, United States, 2018. doi: 10.2514/6.2018-3138.
- [16] Yannick D. Mayer, B. Zang, and Mahdi Azarpeyvand. Design of a Kevlar-Walled Test Section with Dynamic Turntable and Aeroacoustic Investigation of an Oscillating Airfoil. In *25th AIAA/CEAS Aeroacoustics Conference*, AIAA 2019-2464, Delft, The Netherlands, 2019. doi: 10.2514/6.2019-2464.
- [17] Hansjörg Streifeneder. Glasfaser-Flugzeug-Service GmbH, 2018. URL <http://www.streifly.de/shopbaender-d.htm>.
- [18] Anca Hatman and Ting Wang. Separated-Flow Transition: Part 1 - Experimental Methodology and Mode Classification. In *ASME 1998 International Gas Turbine and Aeroengine Congress and Exhibition*, 98-GT-461, Stockholm, Sweden, 1998. American Society of Mechanical Engineers.